Atmos. Chem. Phys. Discuss., 5, 1067–1114, 2005
www.atmos-chem-phys.org/acpd/5/1067/
SRef-ID: 1680-7375/acpd/2005-5-1067
European Geosciences Union

Atmospheric Chemistry and Physics Discussions

Physical aerosol properties and their relation to air mass origin at Monte Cimone (Italy) during the first MINATROC campaign

R. Van Dingenen, J.-P. Putaud, S. Martins-Dos Santos, and F. Raes

European Commission, Joint Research Centre, Institute for Environment and Sustainability, I-21020 Ispra (VA), Italy

Received: 13 August 2004 – Accepted: 21 September 2004 – Published: 25 February 2005

Correspondence to: R. Van Dingenen (rita.van-dingenen@jrc.it)

© 2005 Author(s). This work is licensed under a Creative Commons License.

Abstract

Aerosol physical properties were measured at the Monte Cimone Observatory (Italy) from 1 June till 6 July 2000. The measurement site is located in the transition zone between continental boundary layer and the free troposphere (FT), at the border between the Mediterranean area and Central Europe, and is exposed to a variety of air masses. Sub-micrometer number size distributions, aerosol hygroscopicity at 90% RH, refractory size distribution at 270°C and black carbon mass were continuously measured. Number size distributions and hygroscopic properties indicate that the site is exposed to aged continental air masses, however during daytime it is also affected by upslope winds. The mixing of this transported polluted boundary layer air masses with relatively clean FT air leads to frequent nucleation events around local noon.

Night-time size distributions including fine and coarse fractions for each air mass episode have been parameterized by a 3-modal lognormal distribution. Number and volume concentrations in the sub-micrometer modes are strongly affected by the air mass origin, with highest levels in NW-European air masses, versus very clean air in the "Arctic" episode. During the dust episode, the coarse mode is clearly enhanced.

The observed hygroscopic behavior of the aerosol is consistent with the chemical composition described by Putaud et al. (2004a), but no closure could be made because the hygroscopic properties of the water-soluble organic matter is not known. The data suggest that WSOM is slightly-to-moderately hygroscopic, and that this property may well depend on the air mass origin and history.

Although externally mixing is observed in all air masses, the occurrence of "less" hygroscopic particles has mostly such a low occurrence rate that the average growth factor distribution mostly appears as a single mode. This is not the case for the dust episode, where the external mixing between less hygroscopic and more hygroscopic particles is very prominent, and indicating clearly the occurrence of a dust accumulation mode, extending down to 50 nm particles, along with an anthropogenic pollution mode.

ACPD

5, 1067–1114, 2005

The presented physical measurements finally allow us to provide a partitioning of the sub-μm aerosol in four non-overlapping fractions (soluble + volatile, non-soluble + volatile, refractory + non-BC, BC) which can be roughly associated with separate groups of chemical compounds (ions, organic matter, dust, BC).

For what concerns the relative contributions of the fractions, all air masses except the free-tropospheric (FT) and Dust Episodes show a similar composition within the uncertainty of the data. The latter two have a significantly higher refractory fraction, which in the FT air mass is attributed to carbonaceous particles, and in the dust episode to a sub-μm accumulation mode of dust.

1. Introduction

The importance of atmospheric aerosols in the Earth's radiative balance is well recognized through numerous field, laboratory and modelling studies that have appeared in the past decade. IPCC (2001) rates atmospheric aerosols as the least understood atmospheric component for what concerns their role in radiative forcing. In particular, the understanding of the aerosol direct forcing by carbonaceous and mineral aerosol is most problematic, mostly due to a lack of knowledge of the optical properties of these compounds, and how these properties depend on the mixing state of the aerosol (Clarke et al., 2004). A thorough description of the aerosol direct effect, involves knowledge of the number size distribution, chemical size distribution, optical and hygroscopic properties of pure and mixed compounds, as well as the mixing state. The same properties are also key to understanding the indirect and semi-direct effects, related to cloud formation, scattering and absorption inside clouds, and cloud lifetime.

The Mediterranean area (Southern Europe and Northern Africa) is a growing area in terms of industry and air pollution. At the same time, it is strongly under the influence of Saharan dust emissions. The vicinity of these two sources may lead to a regional mixed plume with modified properties compared to the non-mixed plumes. E.g. it is documented (Avila et al., 1997; Loye-Pilot et al., 1996; Casado et al., 1992) that the

ACPD
5, 1067–1114, 2005

acidity of rain in southern Europe is considerably modified by the capacity of mineral dust to neutralize it. This in turns depends on the chemical history of the mineral dust and specifically its calcite content, which can be severely depleted after transport through polluted regions and interaction with H_2SO_4 and HNO_3. It is also likely that through such interactions the export of pollutants from S. Europe and N. Africa and their effect on the global atmosphere will be modified [Dentener et al., 1996]. In particular the atmospheric residence time of pollution and the radiative effect of pollution aerosols are expected to be modified by the degree of mixing of those aerosols with dust, complicating e.g. estimation of the future impact on climate of increasing emissions of SO_2 by developing countries [Andreae and Crutzen, 1997].

This study presents results from a one-month intensive measurement campaign, carried out at Monte Cimone (Italy, 44°11′ N–10°42′ E, 2165 m a.s.l.) as part of the MINATROC (MINeral dust And TROpospheric Chemistry) project. The measurement site is described in companion papers (e.g. Putaud et al., 2004a; Balkanski et al., 2003). The Monte Cimone Station (MTC) is ideally located to monitor aged, well-mixed continental air masses with a large variety in origin and history, basically overlooking most of Europe, the Mediterranean and Northern Africa.

Here we focus on aerosol physical characterisation which was performed simultaneously with gas-phase, aerosol chemical and optical measurements at the same location, results of which are presented in the present issue. This characterisation encompasses measurement of the number size distribution, hygroscopicity, volatility and black carbon content. This dataset yields information on mixing state and contribution of various aerosol classes (soluble/non-soluble/refractory/BC) which will be confronted with chemical data (Putaud et al., 2004a). Aerosol properties will be parameterized according to the air mass category they belong to.

ACPD
5, 1067–1114, 2005

2. Experimental set-up

On-line instruments were located in a laboratory from which a main sample tube (14 cm diameter) passed vertically to the outdoors platform above, from where it extended another 5 m vertically. The inlet was fitted with a PM10 sample head. Inside the laboratory, several secondary sample lines were connected to this central sampling tube leading to various instruments for physical and chemical aerosol characterisation. The major flow rate through the central tube was 500 l/min, of which 350 l/min taken with a mass-flow controlled blower, and 150 l/min by a nephelometer installed at the end of the main sample tube.

Aerosol number size distributions in the 0.006–0.6 μm size range were measured with a custom-built Vienna type DMA (length 28 cm), using a TSI CPC model 3010 as particle counter. The temperature difference between saturator and condenser in the CPC was enhanced to 23°C (in stead of the manufacturer setting of 17°C) in order to improve the detection efficiency in the <10 nm size range (Mertes et al., 1995). The DMA sheath air (7.5 l/min) was re-circulated, filtered, and dried in a closed loop arrangement (Jokinen and Mäkelä, 1997) using a diaphragm pump (KNF model N 035 AN.18). The humidity of the sheath air was kept below 15%. With perfectly equilibrated sheath and excess airflows, the DMA aerosol sample flow rate equals the counter flow rate (1 l/min). The flow rates of this and all other DMA systems were monitored by measuring the pressure drop over a flow restrictor and calibrated daily with a soap bubble flow meter.

Number size distributions in the size range 0.3–10 μm were measured in 15 size classes with an optical particle counter (OPC, GRIMM model 1.108). The optical arrangement inside the instrument is such that the scattered light is detected at an angle of 90°. Unlike the DMA sampling, the aerosol entering the OPC was not dried before entering the instrument. Intercomparison between DMA and OPC data in the overlapping size range (300–600 nm) however shows no systematic size shift in the latter, indicating that the relative humidity inside the OPC is low enough (due to dissipated

ACPD
5, 1067–1114, 2005

heat and the temperature difference between outside air and laboratory) to dry the particles. A linear regression between hourly averaged integrated number concentration and aerosol volume for the overlapping size range of both instruments, shows that particle counts are practically equal (slope = 1.03 ±0.02, 95% CL) whereas the OPC aerosol volume is slightly lower than the volume calculated from DMA (slope = 0.85±0.02, 95% CL). DMA and OPC size distributions are then used to calculate integrated number and aerosol volume for the fine (particle diameter < 1 μm) and coarse (particle diameter >1 μm) fractions.

The aerosol volatility was measured by leading the air sample (1 l/min) through a quartz tube (20 cm length; 1.5 cm inner diameter) in a tube furnace, continuously operated at T=300°C, in front of a second DMA where the resulting size distribution is measured. The operating temperature was chosen in order to remove H_2SO_4, ammonium nitrate, sulfate, bisulfate, and semi-volatile organic compounds. The remaining aerosol at T=300°C is commonly referred to as "refractory" aerosol and may contain non-volatile organic carbon, elemental carbon, sea salt and mineral dust (e.g. Clarke, 1991; Kreidenweis et al., 1998). The size distributions of the heated and ambient samples were measured simultaneously and with identical systems. Laboratory tests with an internal mixture of sodium chloride and ammonium sulfate have shown that the tube furnace arrangement is able to evaporate volatile compounds without re-nucleation. Particle losses in the tube furnace were regularly checked by comparing the size distributions of the ambient and volatility DMA with furnace switched off. This indicated that under otherwise identical conditions, the aerosol number and volume measured by the volatility DMA were 78(±5)% and 79 (±6)%, respectively, of the values obtained with the ambient DMA. Reported refractory number and volume have been corrected for this difference. On a few random occasions during the campaign, the hygroscopicity of this refractory aerosol was measured with the humidity Tandem-DMA (see below). These measurements showed that the refractory aerosol was completely insoluble, indicating that salts were not significantly present.

Aerosol hygroscopicity was measured with a tandem system of two custom built

Vienna-type DMAs, identical to the ones used for ambient and refractory size distributions. Both DMA's use a closed loop arrangement, re-circulating the sheath air over a RH conditioner and filter. The equilibration of the aerosol particles with dry or humidified air happens inside the respective DMA's, where the particles travel through the dry and humidified sheath air, respectively. The sheath air of the first (dry) DMA is dried by passing the flow through an absorption drier cartridge which is replaced and regenerated when the RH approaches 15% (typically once every 24 h). In the second DMA, the sheath air is humidified using a Nafion humidifier (Permapure model PH-060-26-12AFS, water in shell). The DMA with humidifier was placed inside a thermally insulated box. At a constant temperature, the humidity of the air leaving the humidifier depends only on the flow rate. With a sheath air flow rate of 7.5 l/min and an ambient temperature of 26°C, a RH of 87%(±2%) was achieved. The hygroscopicity was measured sequentially for dry diameters 50 nm, 100 nm and 200 nm. During each measurement, the dry diameter $D_{p,\mathrm{dry}}$ is selected and kept constant in the first (dry) DMA while the second (humid) DMA measures the transmitted particle concentration as a function of the "wet" diameter, scanning from $0.9D_{p,\mathrm{dry}}$ to $2D_{p,\mathrm{dry}}$ in 50 classes in 5 min. The ratio $D_{p,\mathrm{wet}}/D_{p,\mathrm{dry}}$ is defined as the hygroscopic growth factor (GF).

Figure 1 shows a typical GF distribution for the TDMA at 87% RH, for ambient aerosol and for the calibration salt ammonium sulfate. The observed spread on the GF is in the first place caused by the instrumental resolution, imposing a minimum width, in our case $\sigma_{g,\mathrm{min}}$=1.07 at 200 nm, as derived for pure ammonium sulfate particles. Hence, completely chemically homogeneous particles (internally mixed with identical composition) would appear as a single GF peak with this minimum width. An increasing chemical heterogeneity results in a widening of the observed GF distribution, and/or the appearance of separate GF modes as has been frequently observed (McMurry and Stolzenburg, 1989; Svenningson et al., 1992; Zhang et al., 1993; Covert and Heintzenberg, 1993; Berg et al., 1998; Swietlicki et al., 2000).

The definition of a GF mode however is not always unambiguous. Figure 2b shows an example of a GF distribution which can be interpreted as a single broad hygro-

ACPD
5, 1067–1114, 2005

scopicity mode with average GF=1.27, σ_g=1.10, or as 2 partly merged modes with respective GF of 1.20 and 1.35, σ_g=1.07, each mode containing 50% of the particles.

In fact, irrespective of the shape of the GF distribution, one can always calculate a geometric mean GF and standard deviation of a GF spectrum with discrete bins GF_i:

$$GF_g = \exp\left(\frac{\sum n_i \ln GF_i}{\sum n_i}\right), \sigma_g = \exp\left(\frac{\sum n_i \left(\ln GF_i - \ln GF_g\right)^2}{\sum n_i}\right)^{1/2}, \quad (1)$$

where n_i = particle counts in bin GF_i.

On the other hand, one can fit one or more lognormal distributions to the observed GF distributions, yielding GF_g and σ_g for each mode. Figure 2 shows examples of one single and three bi-modal lognormal GF distributions with modal σ_g=1.07 and variable separation (full line), together with a single-mode lognormal GF distribution with parameters according to Eq. 1 (dotted line). Obviously, for a single mode, Eq. 1 leads to the correct parameters to give the lognormal distribution (Fig. 2a). When more modes are present, σ_g from Eq. (1) will exceed the minimum $\sigma_{g,\min}$ and the individual mode σ_g's. Hence, σ_g from Eq. (1) in fact holds information on the chemical heterogeneity of the sample.

A visual analysis of bimodal model GF distributions with varying number and separation, shows that, when 2 modes with $\sigma_{g,i}$=1.07 are present, they are recognizable when the average $\sigma_g \geq 1.10$. Hence, for the analysis of our hygroscopicity measurements we proceeded as follows:

- Growth factor spectra for each diameter are combined into hourly averages.
- Equation (1) is applied to calculate GF_g and σ_g for hourly averages of measured GF distributions.
- Data (hourly averages) where $\sigma_g \geq 1.09$ are visually inspected and if 2 modes can be distinguished, a bimodal fit is applied to obtain GF and σ_g for each mode.

ACPD
5, 1067–1114, 2005

– When only one mode is obtained, it is assigned to the "more hygroscopic" class.

All reported data are then recalculated to represent hygroscopicity at 90% RH, assuming ammonium sulfate as the model salt for the soluble fraction and a GF=1 for the non-soluble fraction (Hämeri et al., 2001). Regardless of the RH, the soluble fraction (as ammonium sulfate equivalent) for a given "monodisperse" GF can be expressed as (Virkkula et al., 1999):

$$\varepsilon_i = \frac{GF^3 - 1}{GF_i^3 - 1} \tag{2}$$

with GF the measured growth factor of the mixed particle and GF_i the growth factor of pure ammonium sulfate at the given RH. Hence, at 90% RH:

$$GF_{90}^3 = \varepsilon_i \left(GF_{i,90}^3 - 1 \right) + 1. \tag{3}$$

For a GF distribution, the calculated soluble fraction (Eq. 2) depends on the definition and resolution of the modes: when more modes are present, applying Eq. (2) with GF from Eq. (1) leads to an underestimation of the soluble fraction compared to a calculation applying Eq. (1) onto each resolved GF mode. Figure 3 shows how this error increases with increasing spread on the GF distribution due to the appearance and increasing separation of 2 modes with σ_g=1.07 and equal number in each mode. For a 2-modal GF distribution with a dominating lower (higher) hygroscopicity mode, the error on the soluble fraction is larger (lower). However, for σ_g<1.10, the error (underestimation of the soluble fraction) remains in any case below 5%.

Calibration of the TDMA system with pure ammonium sulfate showed that, without humidification in DMA2, a GF of 1 was found. With humidification to 88.5%, a systematic under-prediction of the GF for 200 (100) nm particles with 15% (12%) was observed, compared to the GF for ammonium sulfate calculated from Tang and Munkelwitz (1994), combined with a correction for the Kelvin effect (Hämeri et al., 2000). Reported data are corrected for this deviation, which is attributed to the fact that the

aerosol flow (1 l/min) was not RH conditioned prior to entering the DMA, as was confirmed a posteriori in laboratory tests.

The black carbon concentration was measured from the same common sample tube with a commercial GIV Aethalometer™ (incandescent lamp) with 15 min time interval and a flow rate of 5 l/min. No pre-conditionning was applied to the sample air. The Aethalometer reports the "Equivalent Black Carbon" concentration (EBC) in ng/m^3 based on an assumed attenuation cross section of the black carbon aerosol filter deposit of 19 m^2 g^{-1}. Comparison between Aethalometer data and elemental carbon (EC) from impactor foils analyzed by Evolved Gas Analysis (EGA, see Putaud et al., 2004a) during this campaign showed a good correlation (R^2=0.71) between the datasets, but with EBC giving only 45% of the impactor results, which indicates a specific attenuation cross section of 8.5 m^2 g^{-1}. Although the thermal method is still being debated, the EBC –EC correction factor lies within the range 1.9–2.5 obtained by Petzold et al. (1997). Hence, we multiplied all Aethalometer EBC concentration data with a factor 2.22 (=1/0.45). An additional correction for the so-called "shadowing effect" (Weingartner et al., 2003) has not been included, because this correction becomes significant only for nearly pure black carbon particles. As shown by Putaud et al. (2004a), in the present study, EC accounts for less than 7% of the aerosol mass.

3. Classification of air masses

Data in this study (and companion papers in this issue) have been interpreted in terms of air mass origin. Three-dimensional back-trajectories arriving at MTC have been calculated using the Lagrangian FLEXTRA model (Stohl et al., 1995). For each day, the model generated eight trajectories based on the meteorological fields produced by the numerical weather prediction model of the European Center for Medium Range Weather Forecast (ECWMF). Each trajectory was obtained for a 10 days length and a 3 h time resolution. All trajectories were visually inspected and classified according to their predominant position over one out of 6 zones over Europe before reaching the

MTC observatory (see Fig. 4).

The following zones were identified for classifying the observations:

1. Arctic; a relatively short but clearly distinct period (during 8 h, 18 July–19 July) corresponded to air masses directly coming from the Arctic zone, transported through the free troposphere, subsiding to the measurement site from original altitude around 6000 m. The trajectory shown in Fig. 4 belongs to this class.
2. North-West Europe; a zone with expected high anthropogenic emissions, in particular nitrogen compounds;
3. Atlantic-West Europe; originating over the Atlantic and passing over land (France) but with less anthropogenic contribution expected than the previous case
4. East European; passing over continental Europe
5. Mediterranean area
6. African continental; originating south of 35° N
    a) Air masses not containing dust
    b) Air masses containing dust (3–4 July), defined by in-situ measured coarse aerosol concentration and by the observation of a dust layer by the LIDAR installed 300 m below the station (Gobbi et al., 2003).

Table 1 shows averaged meteorological parameters for these episodes. Note the low RH for the Arctic episode, and the high T during dust.

4. Results and discussion

Figure 5 shows a time series of the sub-micron aerosol volume (V_f) and super-micron aerosol volume (V_c, size range 1–10 μm), the integrated number concentration in the

DMA size range (N_{tot}), the integrated number concentration for particles smaller than 20 nm (N_{20}), and the equivalent black carbon concentration (EBC). Yellow and blue points indicate daytime (08:00–18:00 UTC) and night time (20:00–5:00 UTC) data, respectively. The time axis refers to local daylight saving time (UTC+2). The figure also indicates the type of air masses arriving at the site, according to the classification described above.

The combined data-set illustrates the occurrence of a long-term variability, linked to air mass history, modulated with a diurnal variability which is particularly evident in N_{20}. The role of air mass origin can be inferred from variations in the night-time 'baseline' of the fine aerosol volume showing higher values in the first half of the measurement period (air masses from NW Europe), and in particular in the coarse aerosol volume during the last 2 campaign days when the site was exposed to transported African dust. In the following, we will discuss both the role of local upslope winds, as well as the role of long range air mass history in determining the physical properties of aerosol particles at Mt. Cimone.

4.1. Diurnal variation and upslope winds

Figure 6 shows average diurnal trends (with 95% confidence level as error bars) for hourly averaged sub-micrometer aerosol total and ultrafine number, aerosol volume V, the equivalent black carbon concentration (EBC), the refractory volume and number fractions f_{Vr} and f_{Nr}, the "average" hygroscopic growth factor at 90% RH of 200 nm and 50 nm particles, and the "average" geometric standard deviation (width) of the GF distribution for both diameters (i.e. both GF and σ_g according to Eq. 1).

Several interesting observations can be made from these average diurnal cycles. First of all, the diurnal trends, already indicated above, appear clearly in the first 3 panels, which are related to extensive (concentration dependent) properties whereas the 3 last panels, referring to aerosol intensive properties (not concentration dependent) do not show this trend. This indicates that the observed changes are rather linked to transport-related phenomena (mixing, dilution) and to a less extend to aerosol

processing. During the night (22:00–07:00 local time) lowest concentration levels are observed. Table 2 summarizes averaged values for aerosol physical parameters in FT conditions for various types of air masses (discussed below), averaged for the time-window 00:00–07:00. It appears that properties related to the fine fraction (absorption coefficient, total number concentration, sub-micrometer volume) are significantly higher than the Alpine Jungfraujoch site which is part of the WMO Central European Global Atmosphere Watch (GAW) background station (Baltensperger et al., 1997) as well as for the North Atlantic FT site of Izaña, Tenerife, Canary Islands (Maring et al., 2000; Van Dingenen, unpublished data). Also the relative humidity at the site remains in general relatively high during the night (>60%), except during the "Arctid" episode, which indicates that the site is not completely decoupled from the boundary layer. In conclusion, most data indicate that during the period of the campaign (June–July) the MTC site, which is at lower altitude than the "nearby" Jungfraujoch site, is actually located in a transition layer between the planetary boundary layer and the free troposphere, where in the course of a diurnal cycle various degrees of mixing between boundary layer and free tropospheric air are observed. In fact, during the measurement campaign, only during the brief Arctic episode, the station appeared to be exposed to pristine free-tropospheric air.

Interestingly, not all aerosol properties can be explained by a linear mixing process between boundary layer and free troposphere, as is illustrated by the trend in ultrafine particles. A remarkably steep increase in the ultrafine particles is observed to start around 11:00, more or less 2 h after the onset of the increase in the absorption coefficient. Whereas the latter must be related to transport (upslope winds, induced by heating of the mountain slopes) by lack of local sources, the sudden increase in ultrafine particles can only be explained by in-situ nucleation. The jump in the number concentration, due to the increase in the ultra-fine size range, is not observed in the volatility DMA system, which indicates that these new particles are not formed on refractory cores, but as new, externally mixed volatile particles evaporating completely at 300°C. The formation of new particles by homogeneous nucleation critically depends

on the balancing between formation in the gas-phase and scavenging by pre-existing particles of condensable compounds.

Figure 7 shows for each particle size bin measured with the DMA, the correlation coefficient with EBC for the complete campaign time series. Clearly, particles in the ultra-fine size range are not correlated with black carbon ($R<0.15$), whereas particles in the accumulation size range (100–300 nm) show a correlation coefficient $R>0.8$. This indicates that the diurnal variation in N_{20} is not simply related to upslope transport, but rather to in-situ photochemically-induced homogeneous nucleation, whereas accumulation mode particles are associated with upslope transport of more polluted BL air. Hence, the transient zone between polluted boundary layer and clean free troposphere seems to favor conditions for new particle formation.

4.2. Characterisation in function of air masses

4.2.1. Size distribution parameters

In what follows we will further characterize the aerosol properties in terms of the air mass origin. Table 2 gives an overview of aerosol number, volume, and equivalent black carbon (EBC) concentrations for the various types of air masses defined before. Only night time data have been included to exclude the influence of local pollution.

Significant differences in sub-μm aerosol volume are observed for different air masses: NW-European air masses, passing over polluted industrial and densely populated areas of the German Ruhr-area, The Netherlands and Belgium have the highest aerosol loading and black carbon level. Number concentrations and sub-micron volume are comparable for W-European, E-European, Mediterranean and non-dusty African air masses. The African-dust case is characterized by a strongly enhanced super-micron aerosol volume, as expected. Very clean air was observed in Arctic airmasses (low number and submicrometer volume), however, taking into account these low levels, this episode is also characterized by a relatively high level of absorbing particles as well as super-micrometer volume. This episode resembles most the conditions of the

North-Atlantic FT observatory at Izaña, Tenerife outside dust episodes (Maring et al., 2000; Van Dingenen, unpublished data).

Averaged number (N), surface (S) and volume (V) size distributions for each of the episodes are shown in Fig. 8. These data have been fit with a 3-modal lognormal distribution, representing very well the sub- and super-micrometer size range. Modal parameters are given in Table 3. Note that the lognormal parameters for S and V have not been obtained independently, but have been calculated from the number size distribution fits, using the Hatch-Choate equations (Hinds, 1982), i.e. for modes i=1, 3:

$$\sigma_{gN,i} = \sigma_{gS,i} = \sigma_{gV,i}$$

$$D_{gS,i} = D_{gN,i} \exp\left(2 \ln^2 \sigma_{gN,i}\right), D_{gV,i} = D_{gN,i} \exp\left(3 \ln^2 \sigma_{gN,i}\right)$$

$$S_i = \pi D_{gN,i}^2 N_i \exp\left(2 \ln^2 \sigma_{gN,i}\right), V_i = \frac{\pi}{6} D_{gN,i}^3 N_i \exp\left[\frac{9}{2} \ln^2 \sigma_{gN,i}\right].$$

Figure 8 shows that these lognormal parameters give a consistent and adequate description of the measured dry size distributions for all three moments.

The distributions are consistent with the air mass classifications: all episodes show a quite similar "background" coarse mode (mode 3) with number mode diameter around 1.5–1.6 μm, and number 0.15–0.30 cm^{-3}, except the dust episode where the average coarse mode number is 4 cm^{-3}. In the latter case, the coarse mode contributes significantly to the sub-micrometer fraction for particle diameters >500 nm.

The accumulation mode (mode 2) shows a larger variability between the episodes with diameter between 135 nm(dust) and 216 nm (NW-EUR), except for the Arctic case where for mode 2 D_{gN}=88 nm. In this case, the 2nd mode is actually much wider (σ_g=1.91) than in the other cases, indicating that it rather consists of 2 merged modes. The highest volume is observed in the NW-EUR accumulation mode. The dust episode has a lower diameter but the highest number in the accumulation mode, indicating a less aged accumulation mode than the other cases (Van Dingenen et al., 2004).

ACPD
5, 1067–1114, 2005

"Aitken" modes (mode 1) have number mode diameters between 50 and 60 nm, except again for the Arctic case where mode (1) corresponds rather to an aged nucleation mode (D_{gN}=16 nm). W and NW-EUR air masses have significantly higher volumes in the Aitken mode than the other episodes.

We believe such parameterizations are useful to establish a climatology of continental size distributions, in particular at higher altitudes where such data are scarce. Comparing modes 1 and 2 of the present dataset with a compilation of sub-μm size distributions for European sites from background to kerbside (Putaud et al., 2003), the MTC distributions generally compare well to European natural background sites in the boundary layer.

4.2.2. Hygroscopicity

Table 4 summarizes the results of the *GF* fitting procedure for the different air masses. The parameters for each hourly spectrum have been combined into number-weighted averages for each air mass episode and each of the 2 *GF* modes (when both available) which we indicate with LH (less hygroscopic) and MH (more hygroscopic).

$$\overline{GF}_m = \frac{\sum GF_{g,m} n_m(GF_g)}{\sum n_m(GF_g)}, m = \text{LH, MH} \quad (4)$$

where n_m (GF) is the particle number in mode m.

A similar averaging procedure was applied to obtain the averaged number fraction of the LH mode and the averaged σ_g of both modes.

Results from the averaged *GF* spectra:

In general, the average *GF* spectrum can be described by one or two modes with $\sigma_g \leq 1.10$. The frequency of occurrence of 2 separate modes (externally mixed aerosol) varies from a few percent (NW-EUR) to 100% of time during dust for 100 and 200 nm particles. Except for the dust event, the occurrence of an externally mixed aerosol is

quite low; this is clearly illustrated in Fig. 9 where normalized (total number = 1) and averaged night time *GF* spectra for each air mass are presented. The number fraction of the "less hygroscopic" mode is calculated as ("fraction of time occurring" × "fraction of particles in separate mode"). Except for the dust event, the overall *GF* spectra appear as a more or less broad single mode. The Arctic case results as 2 modes merged into one very broad mode. Some features are discussed in more detail below.

GF of dusty aerosol:

The contribution of a less hygroscopic (LH) mode for the dusty air mass is very clearly increasing from 50 to 200 nm, with even a dominant contribution in the latter case. Only in this air mass type we observe LH particles occurring 100% of the time (for 100 and 200 nm sizes). This is a very strong indication for the occurrence of externally mixed dust in the accumulation mode. The *GF* of the dust particles is consistent for 100 and 200 nm (1.15–1.17). During the same episode, LH 50 nm particles are observed 86% of time with a *GF* of 1.29. This frequency of occurrence is still much higher than for the other episodes, suggesting that small dust particles are contributing to the 50 nm LH mode, however the higher *GF* indicates that they are internally mixed with soluble material. The large fraction of LH particles in the sub-micron size range cannot be explained by the 'small end tail' of a coarse (dust) mode, as results from the number size distributions (Fig. 8). Hence, we conclude that a dust-rich accumulation mode is transported along with the coarse dust mode.

Relation chemical heterogeneity – *GF*

Figure 9 shows that in all cases and for all sizes, except for the dust episode, a wider distribution (lower maximum value), indicating a larger chemical heterogeneity, is associated with a higher *GF*. Furthermore, for a given air mass, there is a clear shift to larger *GF* at 200 nm, compared to the *GF* distributions for 50 and 100 nm

particles. This may indicate that a process, responsible for adding soluble material, also leads to a diversification in the chemical composition. This would be the case for cloud processing, where some of the particles of a given size may have been activated as CCN, and others not. Condensation on the other hand would lead to a more homogeneous chemical composition of the given size fraction. This interpretation is supported by the fact that the separation between 'narrow' and 'broad' GF spectra is less pronounced for the 50 nm particles, which, for a given supersaturation, are more difficult to activate to cloud droplets than 100 and 200 nm particles. The spectra of the 200 nm particles would then indicate that air masses from Africa and Eastern Europe have experienced less cloud processing than the other ones. The "Arctic" case appears to behave differently, with the distribution broadening towards the less-hygroscopic side with increasing diameter, and practically no shift in the more hygroscopic peak. Air mass trajectories (originating in the upper free troposphere) and low RH indicate the absence of any cloud processing. The 200 nm particles appear to show the largest chemical heterogeneity of the 3 sizes, characterised by 2 broad hygroscopicity modes centred around GF=1.21 and GF=1.47, respectively (see also Table 4). As the presence of dust is practically excluded for this case (see the low coarse mode in Fig. 8), data suggest that hydrophobic organic and/or elemental carbon may contribute significantly to the observed particle population. This will be further discussed below.

Soluble fractions

Figure 10 shows soluble fractions (Eq. 2) obtained from the averaged hygroscopicity spectra for each episode and each size. For all cases, except dust, the 200 nm particles contain the highest soluble fraction of the 3 sizes. However, for the Arctic case the increase in soluble fraction compared to the smaller sizes is much less than for the other episodes, while the Arctic 50 and 100 nm particles contain the highest soluble fractions of all cases. This indicates that for the latter case, condensation, rather than

cloud processing, has been the major process in adding soluble material to the particles, which is consistent with the air mass trajectories for this case, subsiding from the upper troposphere without passage in the boundary layer.

We recall that our calculation assumes that the soluble fraction behaves like ammonium sulfate, which may not be the case a priori. Putaud et al. (2004a) have performed a chemical mass balance for the various episodes during this campaign, and found that in the sub-micron size range, the ionic fraction consists of ammonium nitrate and ammonium sulfate. Chan et al. (1992) have shown that the hygroscopic behaviour of ammonium nitrate is practically equal to that of ammonium sulfate. Hence, for the ionic fraction, the assumption of ammonium sulfate as model salt is justified. Apart from major ions, Putaud et al. (2004a) quantified water-soluble organic matter (WSOM), non-water-soluble organic matter (NWSOM), elemental carbon, dust and a minor remaining unidentified fraction. Of these components, WSOM (accounting for 16 to 32% of the sub-μm mass) may contribute to the hygroscopicity of the aerosol. If WSOM is less hygroscopic than ammonium sulfate, the soluble fraction derived from the GF (with ammonium sulfate as model salt) will be underestimated and vice versa.

The diamonds in Fig. 10 show the soluble fraction calculated from the Putaud et al. (2004a) dataset, assuming only ions are responsible for the particle hygroscopicity (black diamonds) or including also WSOM as a hygroscopic component with similar properties as ions (white diamonds). No separate chemical data are available for the Arctic and non-dusty African episodes. The red circles represent the distribution-averaged soluble fraction from the hygroscopicity data, by weighing the values of 50, 100 and 200 nm soluble fractions according to the contribution of these size fractions in the sub-μm volume (Table 5).

Figure 10 shows that the soluble fraction from the hygroscopicity data is well correlated with the chemistry data, and that, except for the dust case, the red dots lie in between the soluble fraction with and without accounting for WSOM. If the red dot coincides with the black diamond (WSOM out), this means that WSOM is not contributing to the hygroscopicity. If the red dot coincides with the grey diamond (WSOM in), it

ACPD
5, 1067–1114, 2005

means that WSOM has the same hygroscopic properties as the ions. An intermediate value implies WSOM with a lower GF than inorganic ions.

The figure shows that in four out of five cases, the hygroscopic behaviour of the sub-μm aerosol is consistent with the chemical composition if a slightly-to-moderately water-soluble organic fraction is taken into account. Only for the dust episode, the measured hygroscopicity is lower than expected from the chemical composition.

4.2.3. Refractory fraction, volatility and BC

The night-time volatile fraction in number and volume are shown in Fig. 11a for the different air masses. The high refractory number fraction indicates that most (60–85%) of the particles appear to contain a refractory core, whereas 7–25% of the volume is non-volatile. Figure 12 shows typical examples of ambient and refractory size distributions outside and during the dust episode. The shape of the refractory size distributions and the shift of the mode towards smaller sizes compared to the ambient distribution, indicates that most particles originally consisted of a refractory core (soot, dust), mixed with semi-volatile components. In terms of refractory cores, the Mediterranean and African air masses appear to be more externally mixed than the other cases.

The highest refractory volume fractions are found for the Arctic and African - dust cases. These are also the cases where hygroscopicity measurements already indicated a significant LH fraction in the sub-μm size range.

Figure 11 also shows the contribution of BC to the sub-μm volume (a) and to the refractory volume (b). The BC volume was calculated from the measured mass (corrected for the actual attenuation cross section, see above) and an assumed density of 2 g/cm^3 (Fuller et al., 1999). The highest (relative) contribution of BC to the sub-μm volume is found in the Arctic case, however with a 100% uncertainty interval on the calculated value, due to the near-detection limit values during that episode. Although the very low RH of the air mass, as well as the air mass trajectories suggest an upper tropospheric origin, the BC mass in this case (62±87 ng m^{-3}, see Table 1) is much higher than values around 2 ng m^{-3} measured in the Northern Hemispheric upper tro-

posphere (Pueschel et al., 1997) and attributed to commercial aviation. If the BC would come with upslope transport from the boundary layer, one would expect to find a BC/V ratio close to the other values reported in the table. In fact, in all other episodes, BC accounts for 5–8% of the submicron aerosol volume, a value which is consistent with observed BL values from the urban background to remote continental sites (Putaud et al., 2004b). Although our BC values for the Arctic case are very uncertain, hygroscopicity and volatility data clearly show the occurrence of a refractory (non-dust), non-soluble fraction which is mixed to various degrees with more hygroscopic material.

For the dust case, it is clear that BC accounts only for a small part (30±5%) of the refractory volume, giving additional evidence for the presence of dust in the sub-micron range.

4.2.4. Aerosol partitioning based on physical measurements

In Table 6 we summarize the partitioning of the sub-μm aerosol for all episodes in 4 fractions, based on the following assumptions:

1. The refractory aerosol is non-soluble, based on the absence of any significant amounts of sea-salt in the sub-μm aerosol (Putaud et al., 2004a) and occasionally measured hygroscopicity of refractory aerosol (GF=1).
2. BC occurs in the sub-μm fraction

In that case, the following non-overlapping fractions can be derived (Fig. 13):

- soluble + semi-volatile (e.g. ammonium salts, H_2SO_4, WSOM,...)
- non-soluble + semi-volatile (non-soluble OM)
- refractory, non-BC (dust, non-volatile OM)
- BC

It has to be noted that also dust contributes to light absorption, albeit with a low mass absorption efficiency. Clarke et al. (2004) obtained a maximum value of $0.009\,m^2g^{-1}$ for Asian dust. Based on the coarse and fine aerosol volume concentrations observed during the dust episode (Table 2) and the contribution of mineral dust in the coarse and fine fraction (73% and 23%, respectively, see Putaud et al., 2004a), dust is estimated to contribute for less than 10% to the "Equivalent BC" mass. This contribution is subtracted from the BC fraction for the dust episode and re-assigned to the refractory dust fraction.

The errors reported in Table 6 are calculated by error propagation theory from the random errors in all measurements (see also Putaud et al., 2004a), added to the 95% confidence level on the mean. The major contribution to uncertainty in the soluble/non soluble partitioning comes from the RH measurement: an initial uncertainty of 3% on RH (at 90%) propagates to 6% uncertainty on the GF and to 17% on the soluble fraction. In the partitioning between refractory BC-non BC, the detection limit and noise of the aethalometer are the major sources of uncertainty. The high uncertainty on the non-soluble-volatile fraction results from the accumulated uncertainties on the volatile and refractory fractions.

Note that the sum of all fractions equals 1, hence the values are not independent: a lower soluble fraction implies a higher non-soluble-volatile fraction and vice versa, and similar for the partitioning between BC and non-BC refractory fraction.

The fractions can be combined with aerosol sub-micron volumes in Table 2 to obtain actual concentrations. Table 6 also gives the mass fractions in major chemical classes obtained from the chemical mass balance in Putaud et al. (2004a). We did not convert the mass fractions into volume fractions because the densities are not expected to vary much, and the fractions (unlike absolute values) would only be slightly affected. We also have combined the WSOM and NWSOM fractions into one class (OM) for this purpose.

Most cases have a volatile, soluble fraction around 50%, except the dust case where this fraction is 32%. The second most important fraction is the volatile-non-soluble

ACPD
5, 1067–1114, 2005

one (30–40%). Only the dust case has a significant fraction of a refractory-non-BC compound which is consistent with the specific origin of the air mass. In the Arctic case a high refractory fraction is observed, but the high uncertainty on the BC concentration in this case does not allow us to separate it in BC and non-BC classes.

The physical partitioning shows interesting agreements with the chemical partitioning: the semi-volatile-soluble fraction compares well to the ion fraction, the volatile-non-soluble matches the OM fraction, as do dust and BC. We do not claim a one-to-one identification between the "physical" classes and the chemical ones; indeed one can argue that the volatile-non-soluble fraction should not include the soluble OM. However, we have shown earlier that even soluble OM may have a low hygroscopicity and behave as insoluble OM. Further, the refractory-non-BC fraction is expected to contain, apart from dust, some non-volatile OM (consistent with the observation that the chemical dust fraction is lower than the refractory-non-BC fraction, except in the Dust episode), but this fraction appears to be minor compared to the volatile part.

5. Summary and conclusions

Aerosol physical properties were measured from 1 June till 6 July 2000 at the Monte Cimone observatory (Italy, 44°11′ N–10°42′ E, 2165 m a.s.l.) as part of the MINATROC campaign. Observed diurnal variability in the aerosol properties is related to upslope wind bringing polluted air from the continental boundary layer to the site (see also Fischer et al., 2003). This mixing process also induces photochemical production of condensable gas-phase species which leads to a nearly daily nucleation event, with particle number concentration peaking in the early local afternoon.

In general, night-time concentrations of aerosols and BC in particular are comparable to the European natural background, although a signature of the air mass history and upwind pollution sources can be observed.

Night-time size distributions (i.e. in absence of the daytime nucleation mode) up to 10 μm for each air mass episode have been parameterized by a 3-modal lognormal

distribution. Number and volume concentrations in the sub-micrometer modes are strongly affected by the air mass origin, with highest levels in NW-EUR air masses, versus very clean air in the "Arctic" episode. During the Dust episode, the coarse mode is clearly enhanced.

The observed hygroscopic behavior of the aerosol is consistent with the chemical composition described by Putaud et al. (2004a), but no closure could be made because the hygroscopic properties of the water-soluble organic matter is not known. Our data suggest that WSOM is slightly-to-moderately hygroscopic, and that this property may well depend on the air mass origin and history.

Although externally mixing is observed in all air masses, the occurrence of "less" hygroscopic particles has mostly such a low occurrence rate (frequency of occurrence × fraction when occurring) that the average growth factor distribution mostly appears as a single mode. This is not the case for the dust episode, where the external mixing between less hygroscopic and more hygroscopic particles is very prominent, and indicating clearly the occurrence of an externally mixed dust accumulation mode, extending down to 50 nm particles. The brief but distinct "Arctic" episode with northerly air, subsiding from the free troposphere without previous 'contact' with the boundary layer, shows a remarkably broad GF distribution, as well as a high refractory fraction which is not attributable to dust. An in-situ source must be responsible for a chemically rather heterogeneous aerosol population with a large carbonaceous fraction (OC and/or EC).

The presented physical measurements finally allow us to provide a partitioning of the sub-μm aerosol in four non-overlapping fractions which can be associated with separate groups of chemical compounds. Considering that the sum of the soluble fraction (based on hygroscopicity measurements) and the refractory fraction (based on volatility measurements) is less than 1, a volatile-non-soluble fraction can be defined which can be tentatively associated with OM. Within the refractory fraction, a BC and non-BC contribution are distinguished. For what concerns the relative contributions of the fractions, all air masses except the Arctic and Dust Episodes show a similar

composition within the uncertainty of the data.

It should be noted that, although we have presented data averaged over longer time periods, each of the techniques used (size distribution, hygroscopicity, volatility and EBC) has a high time resolution (some minutes) and has the advantage of yielding on-line data. DMA measurements further have a very high sensitivity compared to chemical analytical techniques. Hence, the applied method to make an aerosol partitioning based on physical measurements can be applied under conditions which are not suited for classical chemical analytical methods (high variability, low concentrations), and can therefore be a very useful tool in e.g. source apportionment studies and intensive aerosol characterization studies. By careful optimisation of the measurements, a reduction of the uncertainties is certainly possible..

Acknowledgements. We gratefully acknowledge the logistic support by the personnel of the Monte Cimone observatory and the excellent collaboration during and after the intensive campaign. This work was supported by the European Commission (DG XII) in the framework of the MINATROC project (EVK2-CT-1999-00003).

References

Andreae, M. O. and Crutzen, P. J.: Atmospheric Aerosols: Biogeochemical sources and role in atmospheric chemistry, Science, 276, 1052–1058, 1997.

Avila, A., Querault-Mitjans, I., and Alarcon, M.: Mineralogical composition of African dust delivered by red rains over northeastern Spain, J. Geophys. Res., 102, 21 977–21 996, 1997.

Balkanski, Y., Bauer, S. E., Van Dingenen, R., Bonasoni, P., Schulz, M., Fischer, H., Gobbi, G. P., Hanke, M., Hauglustaine, D., Putaud, J. P., Stohl, A., and Raes, F.: The Mt. Cimone, Italy, free tropospheric campaign: principal characteristics of the gaseous and aerosol composition from European pollution, Mediterranean influences and during African dust events, Atmos. Chem. Phys. Discuss., 3, 1753–1776, 2003, SRef-ID: 1680-7375/acpd/2003-3-1753.

Baltensperger, U., Gäggeler, H. W., Jost, D. T., Lugauer, M., Schwikowski, M., Weingartner, E., and Seibert, P.: Aerosol climatology at the high-Alpine site Jungfraujoch, Switzerland, J. Geophys. Res., 102, 19 707–19 715, 1997.

Bonasoni, P., Cristofanelli, P., Calzolari, F., Bonafè, U., Evangelisti, F., Stohl, A., ZauliSajani, S., Van Dingenen, R., Colombo, T., and Balkanski, Y.: Aerosol-ozone correlations during dust transport episodes, Atmos. Chem. Phys., 4, 1201–1215, 2004, SRef-ID: 1680-7324/acp/2004-4-1201.

Berg, O., Swietlicki, E., and Krejci, R.: Hygroscopic growth of aerosol particles in the marine boundary layer over the Pacific and Southern Oceans during the First Aerosol Characterisation Ecperiment (ACE1), J. Geophys. Res., 103, 16 535–16 545, 1998.

Casado, H., Encinas, D., and Lacaux, J. P.: The moderating effect of the Ca_2^+ ion on the acidity in precipitation, Atmos. Env., 26A, 1175, 1992.

Chan, C. K., Flagan, R. C., and Seinfeld, J. H.: Water activities of $NH_4NO_3/(NH_4)_2SO_4$ solutions, Atm. Env., 26A, 1661–1673, 1992.

Clarke, A. D.: A Thermo-optic technique for in-situ analysis of size-resolved aerosol physicochemistry, Atmos. Env., 25A, 3/4, 635–644, 1991.

Clarke, A. D., Shinozuka, Y., Kapustin, V. N., Howell, S., Huebert, B., Doherty, S., Anderson, T., Covert, D., Anderson, J., Hua, X., Moore II, K. G., McNaughton, C., Carmichael, G., and Weber, R: Size distributions and mixtures of dust and black carbon aerosol in Asian outflow: physiochemistry and optical properties, J. Geophys. Res. 109, D15S09, doi:10.1029/2003JD004378, 2004.

Covert, D. S. and Heintzenberg, J.: Size distributions and chemical properties of aerosol at Ny Alesund, Svalbard, Atmos. Environ., 27, 2989–2997, 1993.

Dentener, F. J., Carmichael, G. R., Zhang, Y., Lelieveld, J., and Crutzen, P. J.: Role of mineral aerosol as a reactive surface in the global troposphere, J. Geophys. Res., 101, 22 869–22 889, 1996.

Fischer, H., Korman, R., Klüpfel, T., Gurk, C., Königstedt, R., Parchatka, U., Rhee, T. S., Brenninkmeijer, C. A. M., Bonasoni, P., and Stohl, A.: Ozone production and trace gas correlations during the June 2000 MINATROC intensive measurement campaign at Monte Cimone, Atmos. Chem. Phys., 3, 725–738, 2003, SRef-ID: 1680-7324/acp/2003-3-725.

Fuller, K. A., Malm, W. C., and Kreidenweis, S. M.: Effects of mixing on extinction by carbonaceous particles, J. Geophys. Res., 104, 15 941–15 954, 1999.

Gobbi, G. P., Barnaba, F., Van Dingenen, R., Putaud, J. P., Mircea, M., and Facchini, M. C.: Lidar and in situ observations of continental and Saharan aerosol: closure analysis of particles optical and physical properties, Atmos. Chem. Phys., 3, 2161–2172, 2003, SRef-ID: 1680-7324/acp/2003-3-2161.

Hämeri, K., Väkevä, M., Aalto, P. P., Kulmala, M., Swietlicki, E., Zhou, J., Seidl, W., Becker, E., and O'Dowd, C. D.: Hygroscopic and CCN properties of aerosol particles in boreal forests, Tellus B, 53, 4, 359–379, 2001.

Hämeri, K., Väkevä, M., Hansson, H.-C., and Laaksonen, A.: Hygroscopic growth of ultrafine ammonium sulphate aerosol measured using an ultrafine tandem differential mobility analyzer. J. Geophys. Res., 105, D17, 22 231–22 242, 2000.

Hinds, W. C.: Aerosol Technology, Wiley and Sons, NY, 1982.

IPCC, Climate change 2001: The scientific basis, Contribution of Working Group I to the third assessment report of the Intergovernmental Panel on Climate Change, edited by Houghton, J. T., Ding, Y., Griggs, D. J., Noguer, M., van der Linden, P. J., Dai, X., Maskell, K., and Johnson, C. A. Cambridge University Press, Cambridge, Unied Kingdom and New York, NY, USA, 881, 2001.

Jokinen, V. and Makela, J. M.: Closed-loop arrangement with critical orifice for DMA sheath/excess flow system, J. Aeros. Sc., 28, 4, 643, 1997.

Kreidenweis, S. M., McInnes, L. M., and Brechtel, F. J.: Observations of aerosol volatility and elemental composition at Macquarie Island during the first Aerosol Characterization Experiment (ACE 1), J. Geophys. Res., 103, 16 511–16 524, 1998.

Loye-Pilot, M. D., Martin, J. M., and Morelli, J.: Influence of Saharan dust on the rain acidity and atmospheric input to the Mediterranean, Nature, 321, 427–428, 1986.

Maring, H., Savoie, D. L., Izaguirre, M. A., McCormick, C., Arimoto, R., Prospero, J. M., and Pilinis, C.: Aerosol physical and optical properties and their relationship to aerosol composition in the free troposphere at Izaña, Tenerife, Canary Islands, during July 1995, J. Geophys. Res., 105, 14677–14700, 2000.

McMurry, P. H. and Stolzenburg, M. R.: On the sensitivity of particle size to relative humidity for Los Angeles aerosols, Atmos. Environ.,23, 497–507, 1989.

Mertes, S., Schröder, F., and Wiedensohler, A.: The particle detection efficiency curve of the TSI-3010 CPC as a function of the temperature difference between saturator and condenser, Aerosol Sci. Technol., 23, 257–261, 1995.

Petzold, A., Kopp, C., and Niessner, R.: The dependence of the specific attenuation cross section on black carbon mass fraction and particle size, Atmospheric Environment, 31, 661–672, 1997.

Pueschel, R. F., Boering, K. A., Verma, S., Howard, S. D., Ferry, G. V., Goodman, J., Allen, D. A., and Hamill, P.: Soot aerosol in the lower stratosphere: pole-to-pole variability and

contribution by aircraft, J. Geophys. Res., 102, 13 113–13 118, 1997.
Putaud, J.-P., Van Dingenen, R., Baltensperger, U., et al.: A European aerosol phenomenology; physical and chemical characteristics of particulate matter at kerbside, urban, rural and background sites in Europe. European Commission, Report nr. EUR 20411 EN, 2003.
Putaud, J.-P., Van Dingenen, R., Dell'Acqua, A., Raes, F., Matta, E., Decesari, S., Facchini, M. C., and Fuzzi, S.: Size-segregated aerosol mass closure and chemical composition in Monte Cimone (I) during MINATROC, Atmos. Chem. Phys., 4, 889–902, 2004a, SRef-ID: 1680-7324/acp/2004-4-889.
Putaud, J.-P., Raes, F., Van Dingenen, R., et al.: A European aerosol phenomenology – 2: chemical characteristics of particulate matter at kerbside, urban, rural and background sites in Europe, Atmos. Env., 38, 2579–2595, 2004b.
Stohl, A., Wotawa, G., Seibert, P., and Kromp-Kolb, H.: Interpolation errors in wind fields as a function of spatial and temporal resolution and their impact on different types of kinematic trajectories. J. Appl. Meteorol., 34, 2149–2165, 1995.
Svenningson, I. B., Hansson, H. C., Widensohler, A., Ogren, J. A., Noone, K. L., and Hallberg, A.: Hygroscopic growth of aerosol particles in the Po Valley, Tellus, 44B, 556–569, 1992.
Swietlicki, E., Zhou, J., Covert, D. S., Hameri, K., Busch, B., Vakeva, M., Dusek, U., Berg, O. H., Wiedensohler, A., Aalto, P., Makela, J., Martinsson, B. G., Papaspiropoulos, G., Mentes, B., Frank, G., and Stratmann, F.: Hygroscopic properties of aerosol particles in the north-eastern Atlantic during ACE-2, Tellus, 52B, 201–227, 2000.
Tang, I. N. and Munkelwitz, H. R.: Water activities, densities, and refractive indices of aqueous sulfates and sodium nitrate droplets of atmospheric importance, J. Geophys. Res. 99, 18 801–18 808, 1994.
Van Dingenen, R., Raes, F., Putaud, J. P., et al.: A European aerosol phenomenology – 1: physical characteristics of particulate matter at kerbside, urban, rural and background sites in Europe, Atmos. Env., 38, 2561–2577, 2004.
Virkkula, A., Van Dingenen, R., Raes. F., and Hjorth, J.: Hygroscopic properties of aserosol formed by oxidation of limonene, α-pinene, and β-pinene, J. Geophys. Res., 104, 3569–3579, 1999.
Weingartner, E., Saathoff, H., Schnaiter, M., Streit, N., Bitnar, B., and Baltensperger, U.: Absorption of light by soot particles: determination of the absorption coefficient by means of aethalometers, J. Aerosol Sci., 34, 1445–1463, 2003.
Zhang, X. Q., McMurry, P. H., Hering, S. V., and Casuccio, G. S.: Mixing characteristics and

water content of submicron aerosols measured in Los Angeles and at the Grand Canyon, Atmos. Environ., 27A, 10, 1593–1607, 1993.

Table 1. Averaged night-time meteorological parameters for different episodes.

	RH (%)	T(°C)	Wind speed(m s^{-1})
ARC	7.0	9.0	11.7
NW-EUR	82.4	6.7	5.2
W-EUR	68.3	7.7	6.7
E-EUR	55.1	9.1	4.9
MED	73.8	8.5	7.4
AFR-NO DUST	89.0	7.6	6.9
AFR-DUST	50.7	14.5	15.4

ACPD

5, 1067–1114, 2005

Table 2. Overview of night time number and volume concentrations (integrated from size distribution measurements) and equivalent black carbon.

	Number (cm^{-3})	Volume D_p<1 μm ($\mu m^3 cm^{-3}$)	Volume D_p>1 μm ($\mu m^3 cm^{-3}$)	Refractory Number D_p<600 nm cm^{-3}	Refractory Volume D_p<600 nm ($\mu m^3 cm^{-3}$)	EBC (ng m^{-3})
Arctic	300±25	0.59±0.03	1.1±0.6	258±21	0.14± 0.02	138±194
W-Europe	2700±230	5.8±1.0	1.7±0.4	2029±253	0.52±0.07	516±35
NW-Europe	4200±650	10.3±1.4	1.7±0.2	3514±538	0.84±0.10	894±66
E-Europe	2200±800	2.9±0.6	2.3±0.6	1359±307	0.41±0.08	314±39
Mediterranean	1900±230	3.2±0.5	2.4±0.9	1304±148	0.37±0.05	422±22
African (no dust)	3000±760	5.0±1.4	2.0±0.6	1553±416	0.36±0.07	540±86
African (dust)	1800±150	5.0±0.3	22.9±8.6	1434±122	1.15±0.19	643±38

Table 3. 3-modal lognormal fit parameters for averaged size distributions for the various types of air masses observed.

mode	N (cm^{-3})	D_{gN} (nm)	S ($\mu m^2 cm^{-3}$)	D_{gS} (nm)	V ($\mu m^3 cm^{-3}$)	D_{gV} (nm)	σ_g
ARCTIC							
1	24	16	0.03	23	0.00	28	1.54
2	284	88	16.00	204	0.67	310	1.91
3	0.13	1622	1.44	2191	0.57	2547	1.47
NW-EUR							
1	3703	60	74	106	1.52	141	1.70
2	752	216	148	291	7.74	338	1.47
3	0.30	1411	3	2347	1.37	3026	1.66
WEST-EUR							
1	2263	61	57	133	1.55	197	1.87
2	651	184	98	260	4.63	309	1.51
3	0.15	1567	2	2693	1.03	3530	1.68
EAST-EUR							
1	1545	48	21	91	0.37	125	1.76
2	521	150	55	225	2.30	277	1.57
3	0.30	1511	3	2352	1.45	2935	1.60
MEDITERRANEAN							
1	1481	59	31	114	0.70	159	1.77
2	468	169	61	245	2.72	295	1.54
3	0.30	1622	4	2597	1.95	3286	1.62
AFRICAN – NO DUST							
1	2325	50	34	93	0.61	128	1.75
2	638	182	92	252	4.19	297	1.50
3	0.32	1496	4	2396	1.60	3032	1.62
AFRICAN – DUST							
1	745	51	11	93	0.20	124	1.72
2	1080	135	112	246	5.33	332	1.73
3	4.00	1500	44	2333	19.12	2910	1.60

ACPD
5, 1067–1114, 2005

Table 4. Statistics of hygroscopic growth factors at 90% RH (night time only) for various air mass episodes.

Dp, dry (nm)	# of hourly averages	frequency of occurrence LH mode	fraction of LH particles*	*GF* (LH)	*GF* (MH)	σ_{LH}	σ_{MH}
ARCTIC							
50	7	14%	51%	1.22	1.37	1.07	1.09
100	7	57%	37%	1.21	1.39	1.07	1.09
200	7	43%	44%	1.21	1.47	1.09	1.10
NW-EUR							
50	22	5%	7%	0.89	1.27	1.03	1.07
100	35	3%	51%	1.18	1.30	1.10	1.08
200	33	6%	3%	0.94	1.47	1.06	1.09
WEST-EUR							
50	47	6%	38%	1.10	1.25	1.07	1.07
100	70	10%	27%	1.24	1.32	1.08	1.08
200	66	5%	38%	1.22	1.46	1.08	1.09
EAST-EUR							
50	35	11%	56%	1.29	1.31	1.06	1.07
100	55	15%	75%	1.40	1.28	1.10	1.08
200	53	19%	35%	1.28	1.41	1.09	1.08
MEDITERRANEAN							
50	87	16%	70%	1.27	1.33	1.07	1.07
100	139	39%	44%	1.24	1.36	1.09	1.08
200	132	39%	34%	1.35	1.50	1.09	1.08
AFRICAN – NO DUST							
50	14	7%	10%	1.16	1.30	1.06	1.07
100	14	57%	29%	1.27	1.31	1.11	1.08
200	14	21%	14%	1.23	1.42	1.07	1.07
AFRICAN – DUST							
50	7	86%	64%	1.29	1.40	1.08	1.05
100	11	100%	44%	1.15	1.35	1.07	1.08
200	12	100%	64%	1.17	1.46	1.08	1.08

* when occurring

ACPD
5, 1067–1114, 2005

Table 5. Weight factors of size ranges contributing to the sub-micron aerosol volume.

	fraction of sub-μm volume in size range		
	<75 nm	75–150 nm	150–1000 nm
ARC	2%	14.0%	84.1%
NW-EUR	2%	9.5%	88.5%
W-EUR	2%	10.6%	87.7%
E-EUR	3%	14.7%	82.3%
MED	2%	12.3%	85.4%
AFR-NO DUST	3%	9.5%	87.9%
AFR-DUST	1%	9.9%	89.0%

Table 6. Partitioning of the sub-μm aerosol volume in fractions based on physical measurements (upper panel) and mass fractions from the chemical mass balance (Putaud et al., 2004a) (lower panel).

	semi-volatile soluble	volatile non-soluble	refractory non-BC	refractory BC
ARC	0.51±0.15	0.24±0.15	0.25±0.04	
NW-EUR	0.58±0.16	0.34±0.16	0.04±0.02	0.04±0.01
W-EUR	0.55±0.16	0.36±0.16	0.05±0.02	0.04±0.01
E-EUR	0.47±0.14	0.39±0.15	0.09±0.04	0.05±0.01
MED	0.59±0.16	0.30±0.17	0.05±0.03	0.06±0.01
AFR-NO DUST	0.49±0.14	0.44±0.15	0.02±0.03	0.05±0.02
AFR-DUST	0.32±0.11	0.46±0.12	0.17±0.04	0.06±0.01
	ions	OM (sol.+ insol.)	dust	BC
ARC	-	-	-	-
NW-EUR	0.56±0.10	0.26±0.04	0.007±0.004	0.047±0.004
W-EUR	0.46±0.06	0.40±0.08	0.018±0.011	0.063±0.007
E-EUR	0.30±0.03	0.50±0.13	0.072±0.038	0.067±0.006
MED	0.51±0.05	0.34±0.08	0.021±0.012	0.048±0.005
AFR-NO DUST	-	-	-	-
AFR-DUST	0.37±0.05	0.23±0.08	0.23±0.19	0.043±0.006

ACPD
5, 1067–1114, 2005

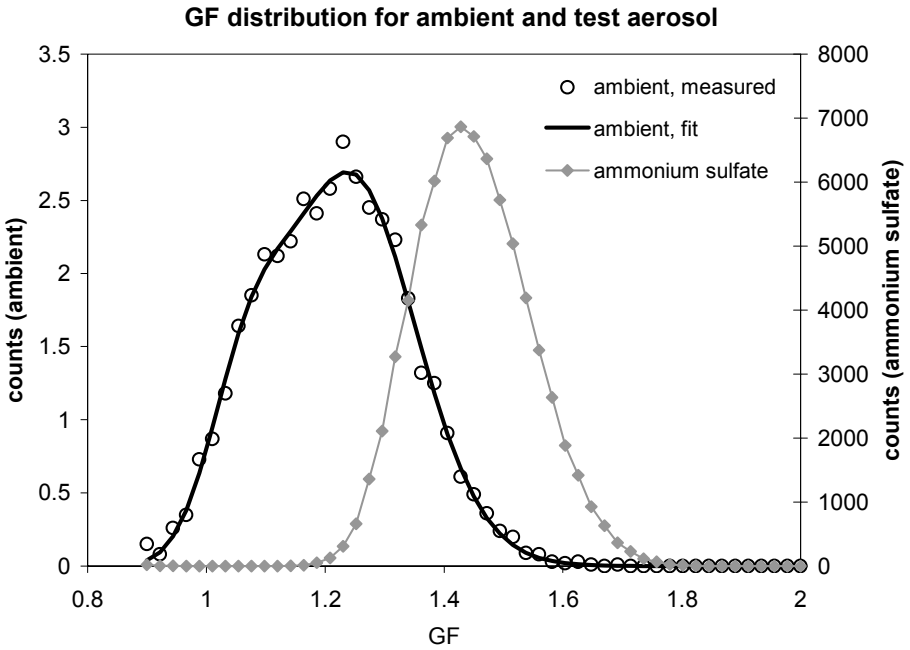

Fig. 1. Hygroscopicity measurement with T-DMA of ambient and test aerosol (ammonium sulfate), together with lognormal fit (full line). The distribution width of the test aerosol is the minimum width of a perfectly internally mixed aerosol.

ACPD
5, 1067–1114, 2005

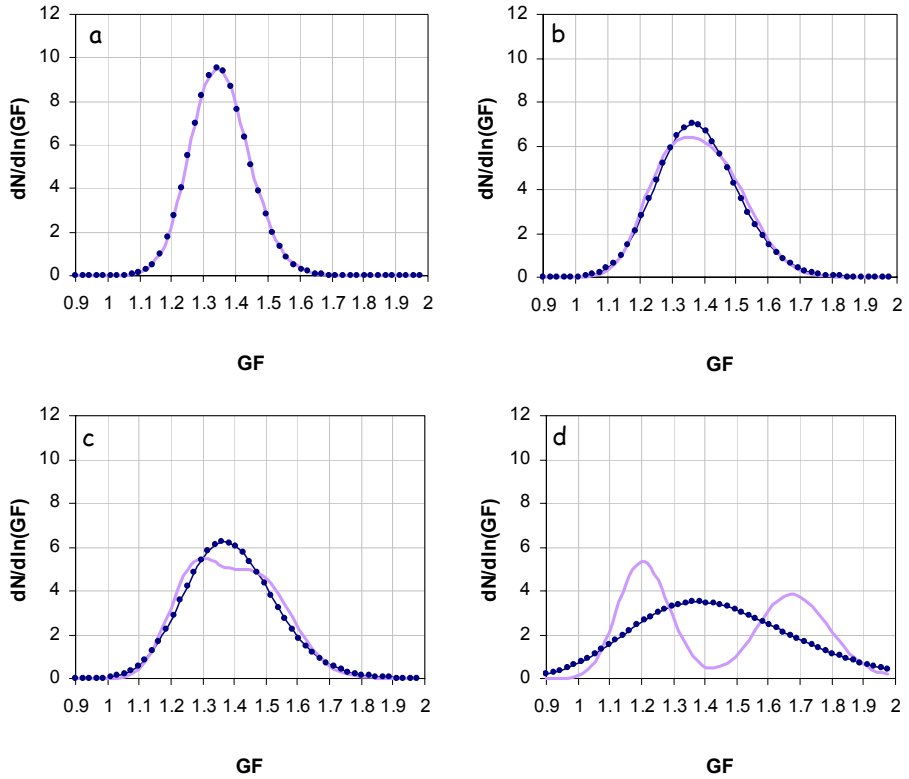

Fig. 2. Analytically generated *GF* distributions from perfectly internally mixed **(a)** to gradually increasing externally mixed **(b)**, **(c)**, **(d)**, by separating the *GF* into two modes with increasing distance (full line, violet). The dotted blue line represents a hypothetical single mode *GF* distribution based on average *GF* and width of the bimodal distributions (see Eq. 1 and text). Case b illustrates the difficulty to recognize two merged modes.

ACPD
5, 1067–1114, 2005

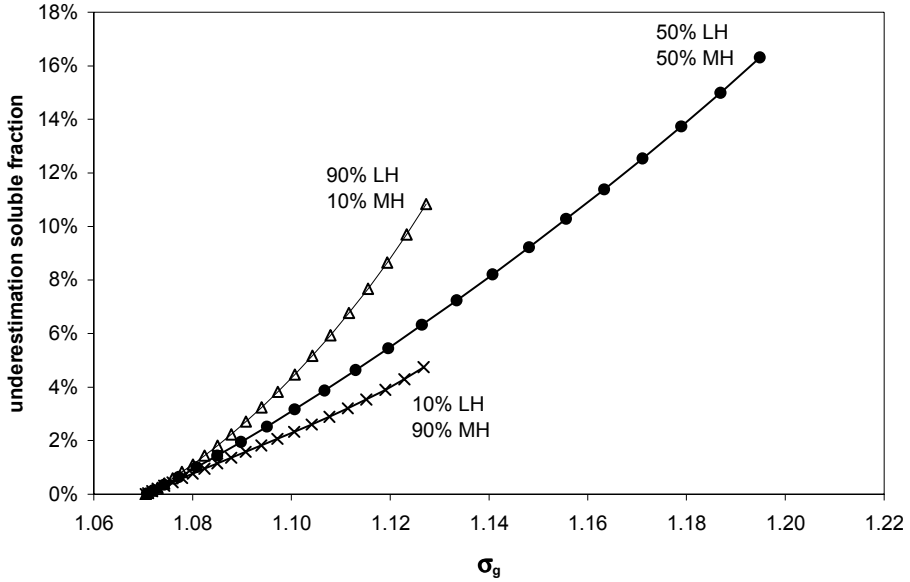

Fig. 3. Calculated error on the soluble fraction (Eq. 2) when a bimodal *GF* distribution (each mode with σ=1.07) is treated as a single lognormal mode, as function of the σ_g of the overall *GF* distribution.

ACPD
5, 1067–1114, 2005

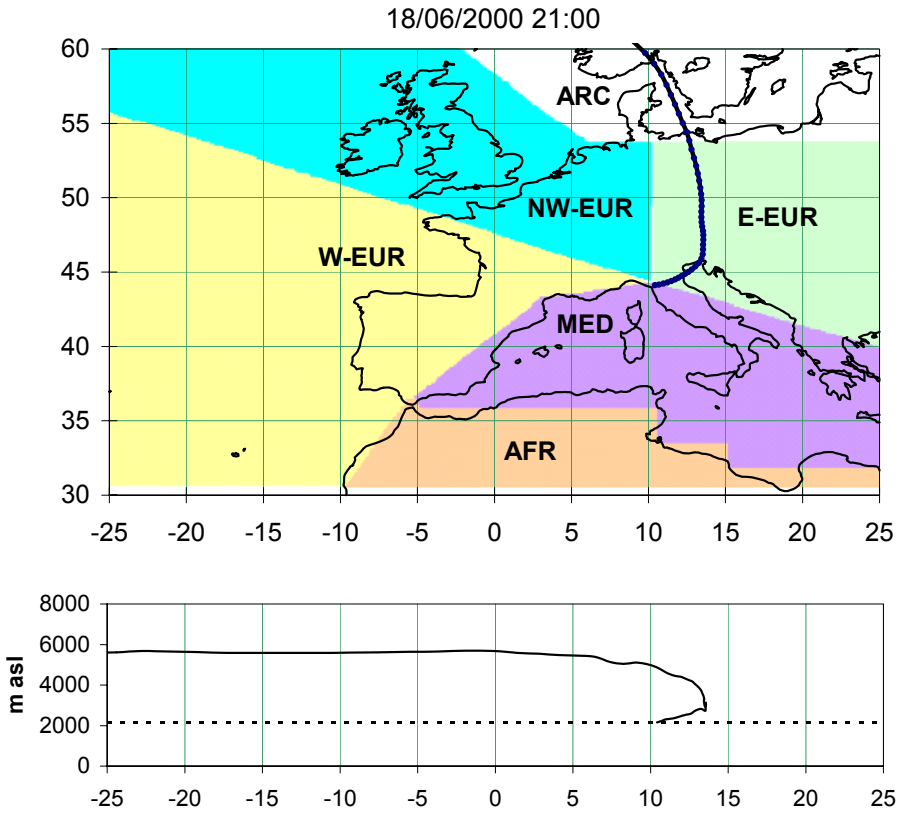

Fig. 4. Identification of the air mass zones for the classification of the trajectories. The trajectory shown on the plot correspond to the "Arctic" class and illustrates the free tropospheric character for this class.

ACPD
5, 1067–1114, 2005

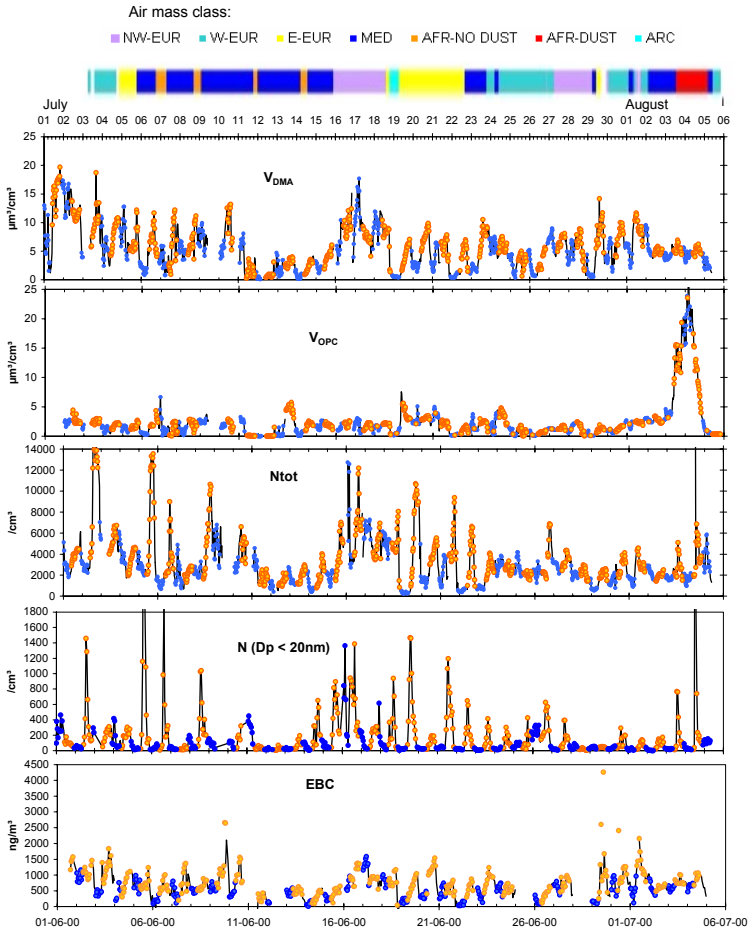

Fig. 5. Time series of various aerosol parameters during the MTC campaign. Yellow dots: day time data; blue dots: night time data. Time axis indicates local time (UTC+2). The colored bar on top indicates the air mass category as a function of time.

ACPD
5, 1067–1114, 2005

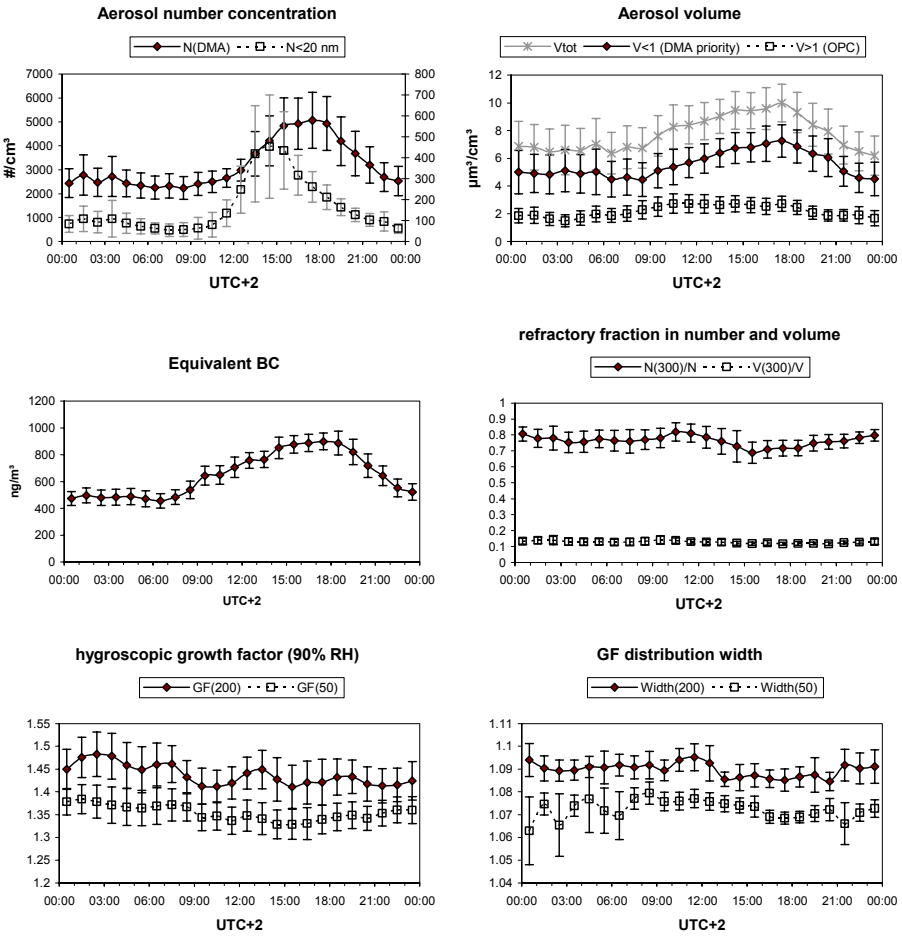

Fig. 6. Average diurnal variation (all data, mean ±95% CL) of aerosol parameters at MTC.

ACPD
5, 1067–1114, 2005

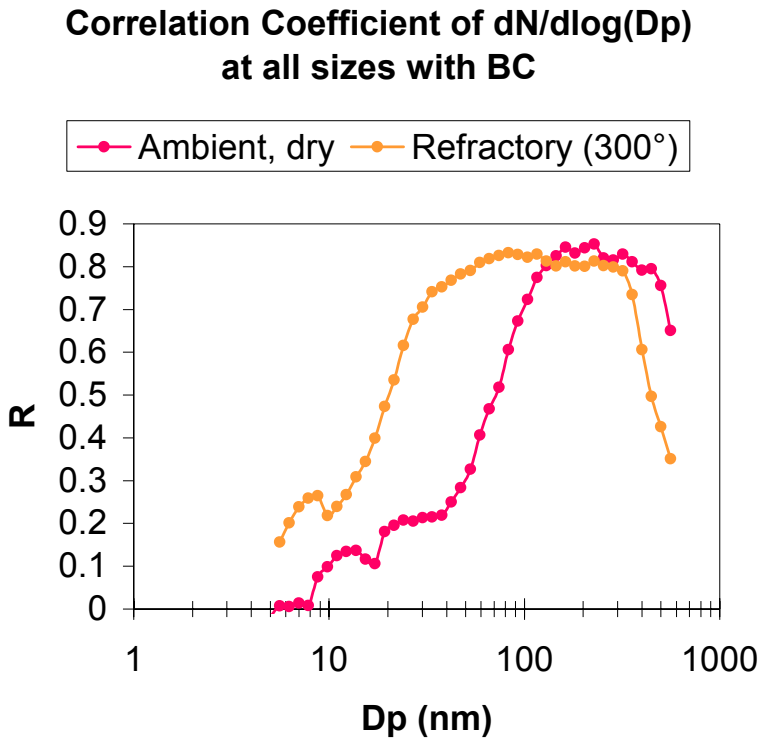

Fig. 7. Correlation coefficient between black carbon concentration and aerosol number within a narrow diameter bin for ambient temperature (red) and refractory aerosol (orange).

ACPD
5, 1067–1114, 2005

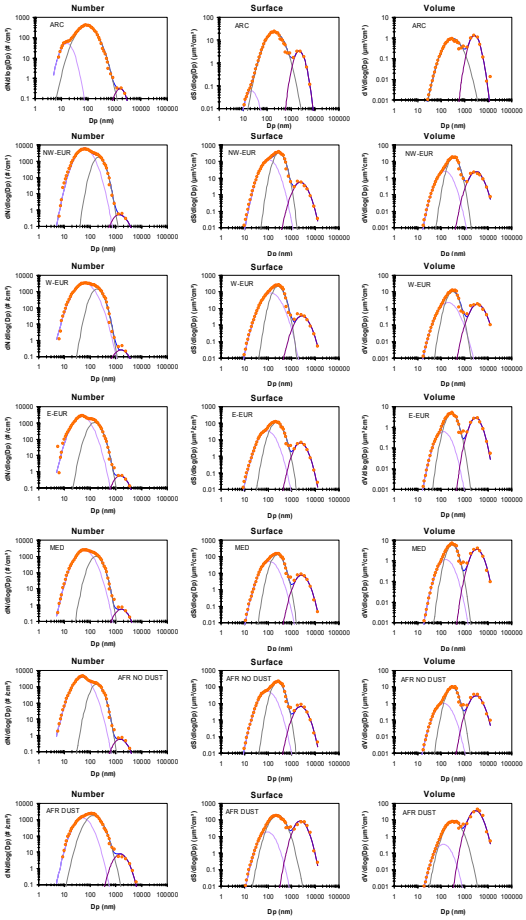

Fig. 8. Averaged number, surface and volume size distributions for the various air masses. Dots: measured averages; full lines: lognormal fits. Parameters are listed in Table 3.

ACPD
5, 1067–1114, 2005

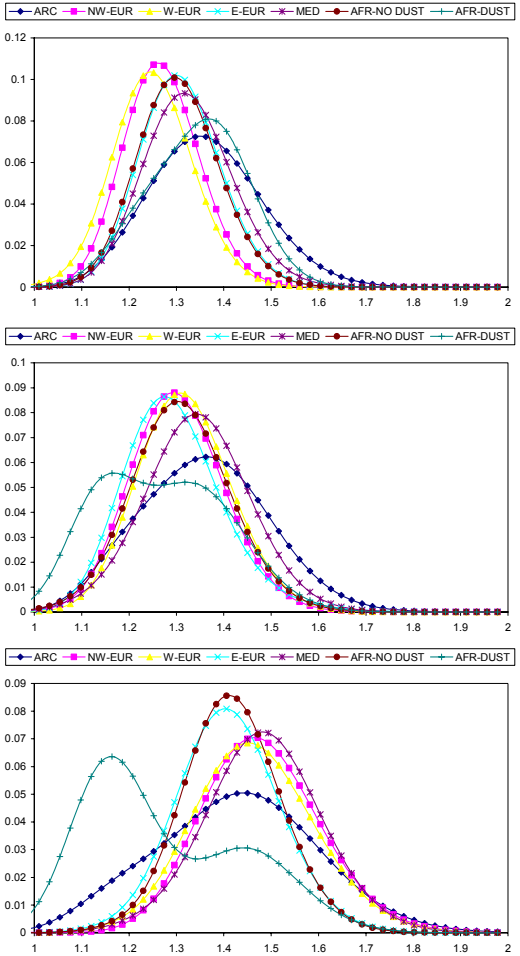

Fig. 9. Averaged normalized lognormal *GF* distributions for the various air masses. Parameters are given in Table 4. **(a)** 50 nm, **(b)** 100 nm, **(c)** 200 nm.

ACPD
5, 1067–1114, 2005

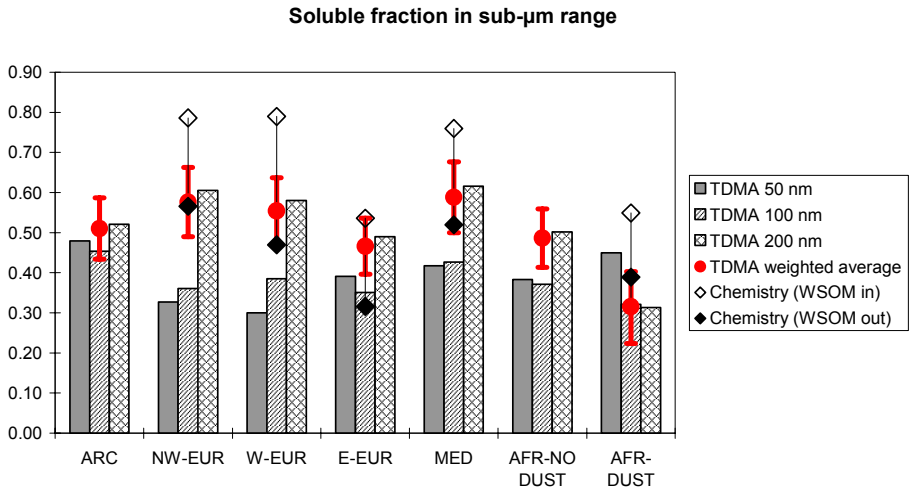

Fig. 10. Soluble fraction calculated from the *GF* measurements for 50, 100, and 200 nm particles (vertical bars), and volume-weighted average for the average size distribution (red dots). White diamonds: soluble fraction calculated from chemical composition, using ions + water soluble organic matter (see text). Black diamonds: idem, excluding water soluble organic matter.

ACPD
5, 1067–1114, 2005

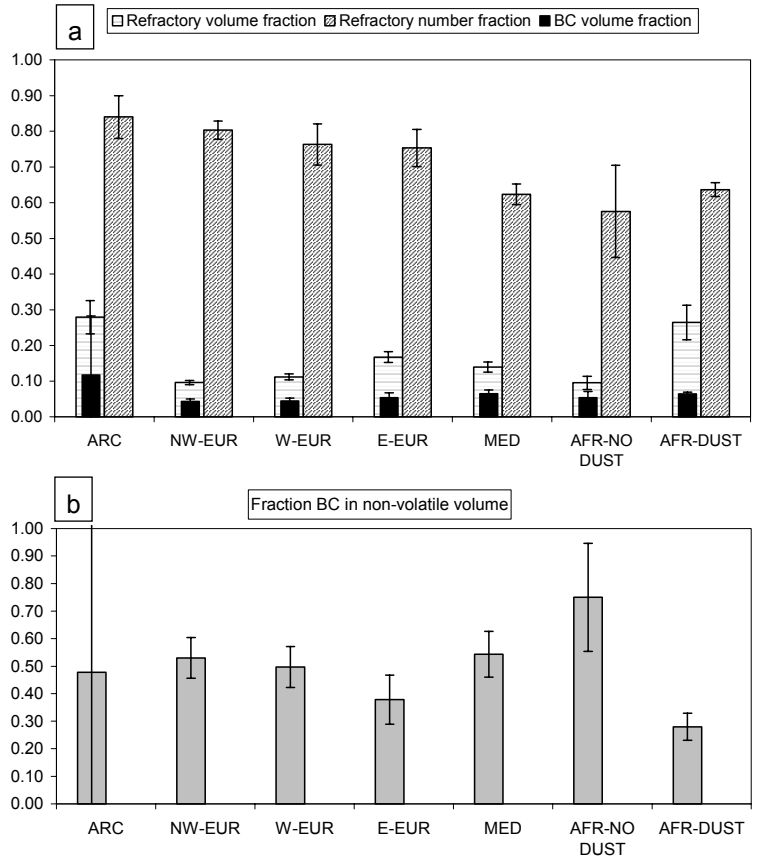

Fig. 11. Refractory number and volume fraction, and BC volume fraction for the different episodes **(a)**; contribution of BC to the refractory fraction **(b)**.

ACPD
5, 1067–1114, 2005

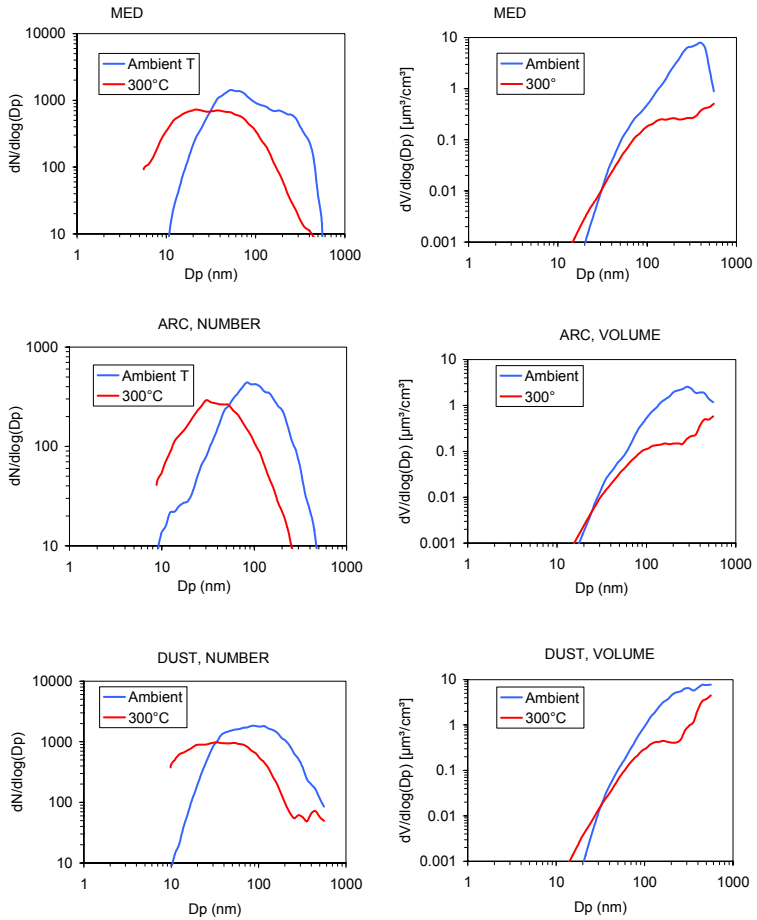

Fig. 12. Examples of ambient and refractory number size distributions.

ACPD
5, 1067–1114, 2005

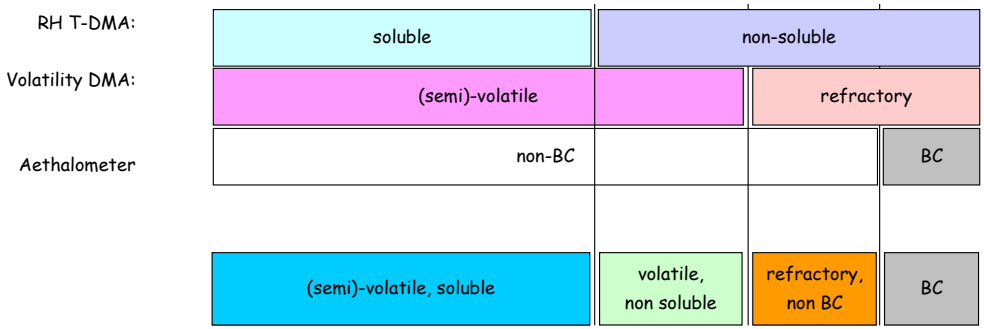

Fig. 13. Scheme for the partitioning of aerosol in four components, based on physical properties measured.

ACPD
5, 1067–1114, 2005